View metadata, citation and similar papers at core.ac.uk
brought to you by CORE
provided by Caltech Authors

Item DR1: Chronology

The chronological framework of the loess-paleosol and red clay sequences is based on paleomagnetic reversal sequences which were detailed in previous studies (Ding et al., 1999; Rutter et al., 1991). Ages of bulk paleosols can be further delineated by bulk soil magnetic susceptibility data (MS), with higher MS values occurring in paleosol units (S) corresponding to interglacial episodes, and lower MS values occurring in loess units (L) corresponding to glacial episodes. The good correlation between the loess-paleosol units and marine isotope stages (MIS) during glacial cycles supports the robustness of this chronology (Rutter et al., 1991). For the current study, bulk paleosol samples collected at 10cm interval were measured on a MS_2 Bartington magnetic susceptibility meter (5% accuracy). The MS data were then tuned to the benthic $\delta^{18}O$ stack LR04 (Lisiecki and Raymo, 2005). Specifically, the top and basal age of each paleosol unit is assigned by the beginning and end of the corresponding interglacial episode (defined by the higher 50 percentiles of $\delta^{18}O$ values), and the ages within a single unit were calculated through interpolation. Both the ages of calcite nodules and finely disseminated calcites were assigned by the ages of the paleosol units they were sampled from.

Item DR2: Carbon isotope analyses

Bulk paleosol samples (~5g) were used for both organic and inorganic $\delta^{13}C$ analyses, and calcite nodule samples (~1g) were only used for inorganic $\delta^{13}C$ analyses. In order to avoid potential contamination of detrital carbonate remaining in the bulk paleosols, as well as authigenic dolomite in the red clay paleosols (He et al., 2012), we identified the types of carbonate minerals (i.e. calcite and/or dolomite) in bulk paleosol samples via the application of Fourier transform infrared spectrophotometry (FTIR), following the methods described in (Ji et al., 2009). For subsequent analysis, we only selected samples for analysis from which dolomite was absent, since its disappearance indicates the complete dissolution of detrital

carbonate (Meng et al., 2015). At least three samples were selected from each paleosol unit which corresponds to a specific interglacial episode.

For measurements of the $\delta^{13}C$ of pedogenic carbonates, splits of bulk paleosol samples as well as nodule samples were first ground into powder and reacted with 10% H_2O_2 to remove organic matter. Oven-dried samples containing ~50 μg of carbonate were then analyzed on either a ThermoFinnigan MAT 253 isotope ratio mass spectrometer, or a Picarro G2131-i cavity ring-down spectrometer. The external precision from replicate analysis of standards is better than ±0.05‰.

For measurements of the $\delta^{13}C$ of SOM, splits of bulk paleosol samples were reacted with excess 1N HCl to remove carbonate, and then rinsed with deionized water multiple times until the pH was neutral. the oven-dried, <5 μm fractions (containing ~50 μg of organic matter) which were separated from the bulk paleosol samples by sieving, were loaded into tin capsules and then analyzed on a ThermoFinnigan MAT 253 isotope ratio mass spectrometer. The external precision from replicate analysis of standards is better than ±0.3‰.

Item DR3: Trace metal measurements

The FDC fractions of bulk paleosol samples from Luochuan and Xifeng sections spanning the last 800-ky interglacials, calcite nodule samples from four Holocene sections (Baoji, Binxian, Luochuan, Yanchang) and Lantian section spanning the last 800-ky interglacials, were applied for trace metal analysis (Mn, Mg, Sr) following methods described in (Li and Li, 2014). In specific, ultrasonically rinsed samples were first reacted with overdosed 0.2 M HNO_3 overnight. The upper dissolvent were then separated from the residuals through centrifugation. The trace metal concentrations of the dissolved product were analyzed on a ThermoScientific iCAP6300 ICP-OES (Inductively Coupled Plasma Optical Emission Spectrometry). Precisions are better than 0.3% for Mn/Ca, Mg/Ca and Sr/Ca following ratio calibration method described in (Li and Li, 2014).

Item DR4: Calculation of the R ratio

For pedogenic carbonate formed in isotopic equilibrium with soil CO_2, the coeval atmospheric pCO_2 can be estimated using a two-component mixing model (Cerling, 1991):

$$pCO_2 = S(z)\ \frac{\delta^{13}C_s - 1.0044\delta^{13}C_r - 4.4}{\delta^{13}C_a - \delta^{13}C_s} \qquad [1]$$

where the subscripts s, r, and a of $\delta^{13}C$ represent the carbon isotopic composition of total-soil CO_2, soil-respired CO_2 and atmospheric CO_2, respectively. The constants of 1.0044 and 4.4 are diffusion coefficients related to different diffusion rates of $^{12}CO_2$ and $^{13}CO_2$.

When all the values of $\delta^{13}C$ in Eq. 2 have been acquired, we can then obtain the R ratio ($pCO_2/S(z)$). Specifically, $\delta^{13}C_s$ can be calculated from $\delta^{13}C_c$ using a temperature-dependent fractionation equation (Romanek et al., 1992):

$$\delta^{13}C_s = \frac{\delta^{13}C_c + 1000}{\frac{11.98 - 0.12T}{1000} + 1} - 1000 \qquad [2]$$

Based on the clumped isotope thermometry, previous work on the CLP have determined little variations the formation temperature of pedogenic carbonates throughout the Pliocene, which is in general 1-2°C lower than modern day summer (JJAS) temperature (Suarez et al., 2011). In the case, we used a -1.5°C correction of average summer temperatures over the past 50 years measured at climate stations nearest to each locality (http://www.geodata.cn/), to present the formation temperatures of our carbonate samples. The standard deviations of the temperatures for each locality were used as 1σ error.

$\delta^{13}C_r$ is usually approximated through $\delta^{13}C$ analysis of coeval SOM. However, significant $\delta^{13}C$ fractionation could occur during the decomposition of SOM (Bowen and Beerling, 2004). SOM occluded in calcite nodules are thought to be buffered against decomposition (Cotton and Sheldon, 2012)). Systematic $\delta^{13}C_{SOM}$ analyses from two Holocene profiles (Luochuan and Binxian) have shown that (Fig. DR5), the $\delta^{13}C$ of SOM occluded in calcite nodules were uniformly more depleted by an

average of -2.34‰, than those in bulk paleosols from the same soil layer where nodules were outcropped. In this case, we applied a correction of -2.34‰ for $\delta^{13}C_{SOM}$ to account for the effect of SOM decomposition.

$\delta^{13}C_a$ can be estimated from the $\delta^{13}C$ of coeval marine carbonate (Tipple et al., 2010b). As the variation of pCO_2 over the last 800 ky is known from ice cores (Lüthi et al., 2008), and pCO_2 estimates during the mPWP generally reaches a consensus of ~400 ppm (Burke et al., 2018), we can solve S(z) by switching the orders of pCO_2 and S(z) in Eq. 2. Standard deviations of ice-core CO_2 records during each interglacial episode (including Holocene) were used as 1σ error. a 1σ error of ±150 ppm was applied for the mPWP- pCO_2, based on the total variations of existing CO_2 records (*ca.* 250-530 ppm).

To propagate errors for all of the inputs in Eq. 2, we applied a MatLab-based PBUQ (paleosol barometer uncertainty quantification) program (Breecker, 2013), which is based on Monte Carlo simulations. Specifically, the program calculates the probability density functions (PDF) of all the variables through 10,000 iterations, based on their input values and associated uncertainties. The program then returns the medians values, and the 16th and 84th percentiles, as the best estimates and 1σ errors of R and S(z).

Item DR5: Calculation of the percent C_4 biomass

The percent C_4 biomass can be estimated by $\delta^{13}C_c/\delta^{13}C_{SOM}$ using a simple two-end-member mixing model (Cerling, 1984):

$$F_{C4}\ (\%) = \frac{\delta^{13}C_i - \delta^{13}C_{C3}}{\delta^{13}C_{C4} - \delta^{13}C_{C3}} \times 100 \qquad [3]$$

where F_{C4} (%) represents the percentage of C_4 biomass, $\delta^{13}C_i$ represents the measured $\delta^{13}C_{SOM}$ values, and $\delta^{13}C_{C4}$ and $\delta^{13}C_{C3}$ are the averaged $\delta^{13}C$ values of pure C_4 or C_3 plant. Here we used the averaged $\delta^{13}C$ values measured from modern day C_3 and C_4 plants on the Loess Plateau (Liu et al., 2005), which is -26.8‰ and -12.5‰, respectively. We also applied a correction of -2.34‰ on the $\delta^{13}C_{SOM}$ to account for the $\delta^{13}C$ fractionation related to degradational process.

Table DR1: Descriptions and statistical results of each sampling locality from this study.

Locality	Latitude (°N)	Longitude (°N)	MAP (mm)	Time interval	$\delta^{13}C_{FDC}$ (‰)	$\delta^{18}O_{FDC}$ (‰)*	$\delta^{13}C_{CN}$ (‰)	$\delta^{18}O_{CN}$ (‰)*	$\delta^{13}C_{SOM}$ (‰)
Weinan	34.50	109.49	552.4	Holocene	-7.0 ± 0.6	NA	-6.2 ± 0.8	NA	-19.4 ± 0.6
Binxian	35.03	108.08	553.2	Holocene	-6.4 ± 0.8	NA	-4.9 ± 0.7	-9.7 ± 0.4	-20.2 ± 0.8
Luochuan	35.77	109.44	621.6	Holocene	-7.5 ± 1.0	NA	-3.6 ± 0.1	-9.7 ± 0.5	-19.8 ± 0.5
Jiaodao	35.98	109.47	576.7	Holocene	-5.6 ± 0.8	NA	-5.0 ± 0.4	NA	-19.7 ± 0.5
Yanchang	36.60	110.01	529.8	Holocene	-5.8 ± 1.5	NA	-4.3 ± 0.3	NA	-19.5 ± 0.2
Lantian	34.15	109.32	719.7	800-ky interglacials	NA	NA	-7.4 ± 1.1	-9.2 ± 0.6	NA
Luochuan	35.77	109.44	621.6	800-ky interglacials	-6.9 ± 1.1	-8.5 ± 0.4	-5.6 ± 0.9	-9.1 ± 0.4	-24.4 ± 1.0
Jiaodao	35.98	109.47	576.7	800-ky interglacials	-7.0 ± 0.8	-9.4 ± 0.4	-5.4 ± 0.9	-9.1 ± 0.3	-23.0 ± 0.6
Xifeng	35.74	107.73	537.0	800-ky interglacials	-6.2 ± 0.9	-8.7 ± 0.5	-5.2 ± 0.7	-9.2 ± 0.3	-22.7 ± 0.7
Lantian	34.15	109.32	719.7	mPWP	-8.7 ± 0.8	-9.7 ± 0.3	-7.8 ± 0.5	-8.7 ± 0.4	-24.7 ± 0.4
Lingtai	35.07	107.62	637.7	mPWP	-7.1 ± 0.6	-9.9 ± 0.6	-7.1 ± 0.9	-9.6 ± 0.3	-25.1 ± 0.4
Xifeng	35.74	107.73	537.0	mPWP	-4.7 ± 0.3	-9.3 ± 0.4	NA	NA	-24.9 ± 0.4
Fuxian	36.01	109.36	576.7	mPWP	NA	NA	-5.1 ± 0.3	-9.0 ± 0.4	-25.1 ± 0.8
Jiaxian	38.03	110.50	433.9	mPWP	NA	NA	NA	NA	-23.8 ± 1.2

*: Some of the Holocene carbonate samples were measured on a Picarro G2131-i cavity ring-down spectrometer, which only generates $\delta^{13}C_c$ data.

Table DR2: Published $\delta^{13}C$ data used in this study.

Reference	Site	Latitude (°N)	Time interval	$\delta^{13}C_c$ (‰)	$\delta^{13}C_{SOM}$ (‰)
(Yang et al., 2015)	Pingliang	35.6	Holocene	NA	-20.2 ± 0.4
(Yang et al., 2015)	Huining	35.7	Holocene	NA	-22.9 ± 0.3
(Yang et al., 2015)	Lanzhou	36.0	Holocene	NA	-23.2 ± 0.5
(Yang et al., 2015)	Puxian	36.4	Holocene	NA	-21.0 ± 0.6
(Yang et al., 2015)	Jingyuan	36.6	Holocene	NA	-23.1 ± 0.3
(Yang et al., 2015)	Hongde	36.8	Holocene	NA	-21.4 ± 0.4
(Yang et al., 2015)	Pianguan	39.5	Holocene	NA	-22.5 ± 0.2
(Gu et al., 2003)	Lingtai	35.1	Holocene	NA	-20.2 ± 0.5
(Gu et al., 2003)	Jixian	36.1	Holocene	NA	-19.7 ± 0.6
(Liu et al., 2005)	Lantian	34.2	Holocene	NA	-19.3 ± 0.8
(Liu et al., 2005)	Xunyi	35.1	Holocene	NA	-20.6 ± 0.6
(Liu et al., 2005)	Xifeng	35.7	Holocene	NA	-19.9 ± 0.6
(Liu et al., 2005)	Huanxian	36.6	Holocene	NA	-23.4 ± 0.6
(An et al., 2005)	Lantian	34.2	800-ky interglacials	-7.9 ± 0.7	-21.2 ± 1.1
(Jiang et al., 2002)	Xifeng	35.7	mPWP	-4.7 ± 0.3	NA
(He et al., 2015)	Jiaxian	38.0	mPWP	-3.4 ± 0.5	NA

Note: Some of the Holocene nodule-$\delta^{13}C_c$ data in Fig.2 and 3 were from Yang et al. (2012). However, detailed information regarding the sampling locations were not provided, and thus not included in this table.

Table DR3: Maximum and minimum R ratios during different time intervals.

Time interval	Finely Disseminated Calcite					
	Location	Min. R	1σ	location	Max. R	1σ
Holocene	Lantian	0.12	+0.14/-0.14	Yanchang	0.57	+0.39/-0.49
Last 800-ky interglacials	Lantian	0.35	+0.16/-0.17	Luochuan	0.75	+0.16/-0.17
mPWP	Lantian	0.56	+0.11/-0.11	Jiaxian	1.54	+0.24/-0.24
Time interval	Calcite Nodule					
	Location	Min. R	1σ	location	Max. R	1σ
Holocene	Weinan	0.41	+0.16/-0.16	Xifeng	0.81	+0.11/-0.12
Last 800-ky interglacials	Lantian	0.40	+0.16/-0.16	Luochuan	0.97	+0.17/-0.17
mPWP	Lantian	0.68	+0.11/-0.11	Fuxian	1.16	+0.17/-0.17

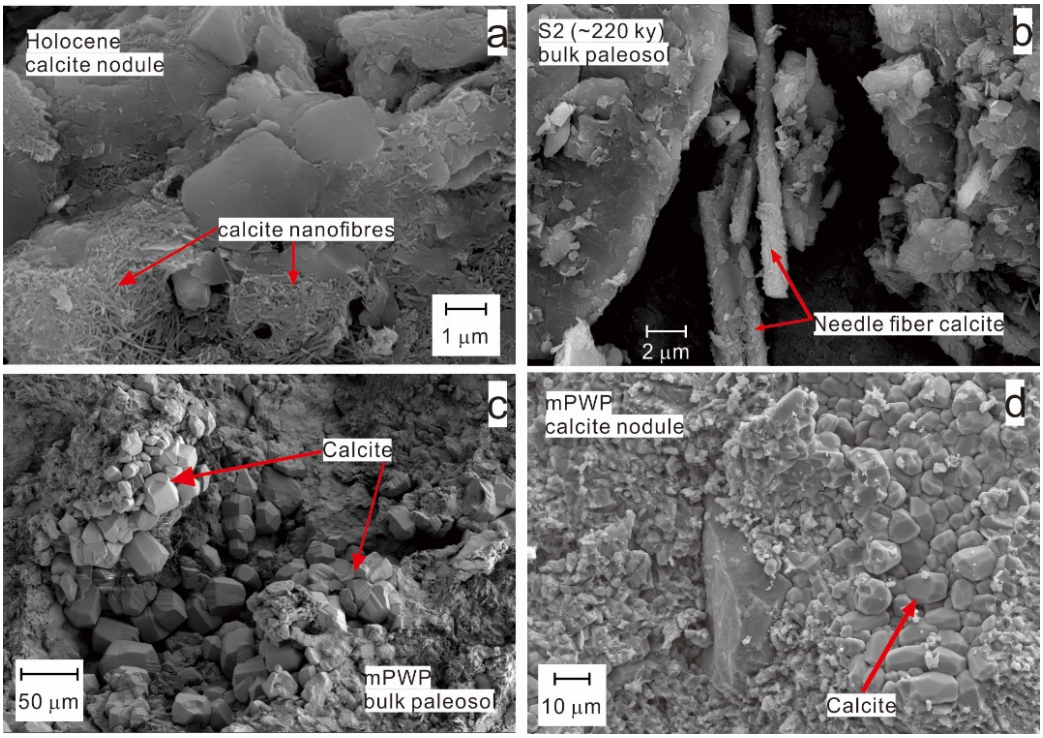

Fig. DR1. Micromorphologies of pedogenic carbonates under scanning electronic microscopy (SEM). (a) Calcite nanofibers in Holocene calcite nodules; (b) Needle fiber calcites in bulk paleosols formed during the MIS 7 interglacial; (c)-(d) Rhombohedral calcite crystals in calcite nodules and bulk paleosols formed during the mPWP.

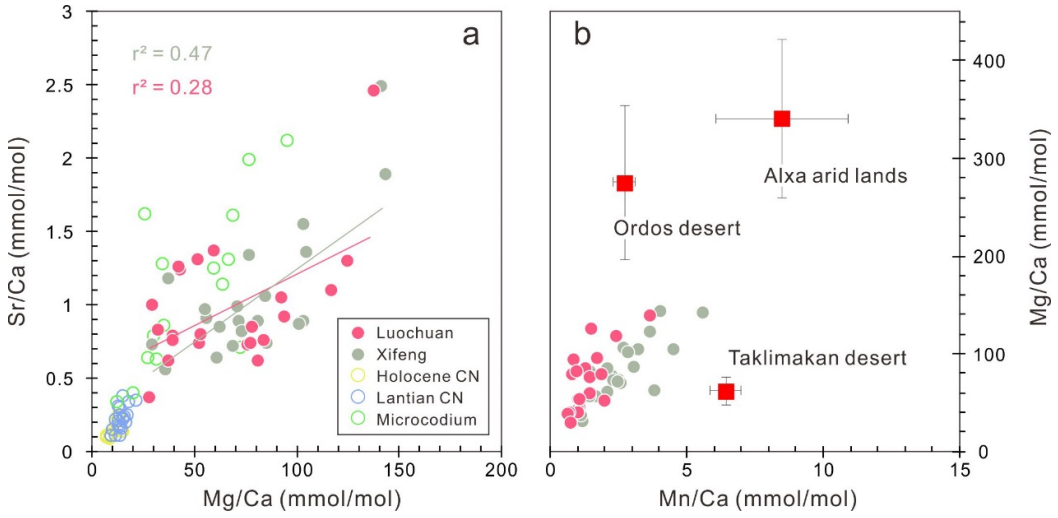

Fig. DR2. Plots of trace element ratios in carbonate fractions. (a) Mg/Ca and Sr/Ca ratios of the FDC fractions in bulk paleosol samples from Luochuan and Xifeng sections spanning the last 800-ky interglacials, the nodule samples from multiple Holocene sections (Baoji, Binxian, Luochuan, Yanchang) and Lantian section spanning the last 800-ky interglacials, and the published Holocene microcodium samples from the Chinese Loess Plateau (Li and Li, 2014). (b) Mg/Ca and Mn/Ca ratios of the FDC fractions in bulk paleosol samples from Luochuan and Xifeng sections spanning the last 800-ky interglacials, compared with those of the carbonate fractions in desert samples collected from potential source regions (Li et al., 2013).

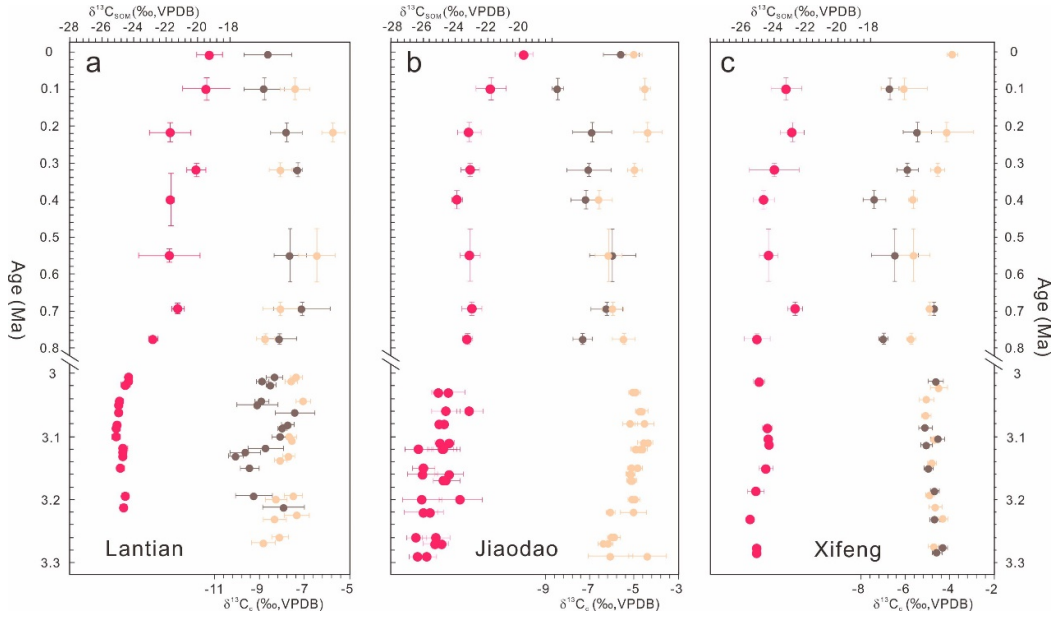

Fig. DR3. Temporal $\delta^{13}C$ variations across the studied time intervals. $\delta^{13}C$ values from (a) Lantian, (b) Jiaodao, and (c) Xifeng are shown separately. Red, grey and yellow dots represent $\delta^{13}C$ data of soil organic matter, finely disseminated calcites and calcite nodules, respectively. Horizontal error bars denote the standard deviations of all the measurements during a specific time interval, and vertical error bars represent the duration of each interglacial episode.

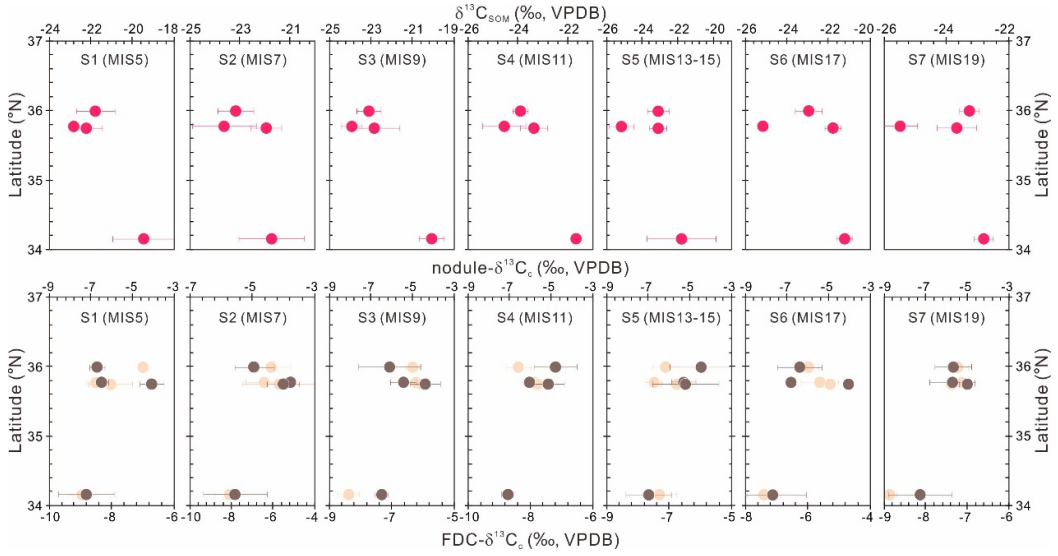

Fig. DR4. Latitudinal $\delta^{13}C$ distributions at each interglacial episode spanning the last 800 ky. Red, grey and yellow dots represent $\delta^{13}C$ data of soil organic matter, finely disseminated calcites (FDC) and calcite nodules, respectively. Error bars denote standard deviations of all the measurements (n≥3) from a single section. Note the different scales for each panel.

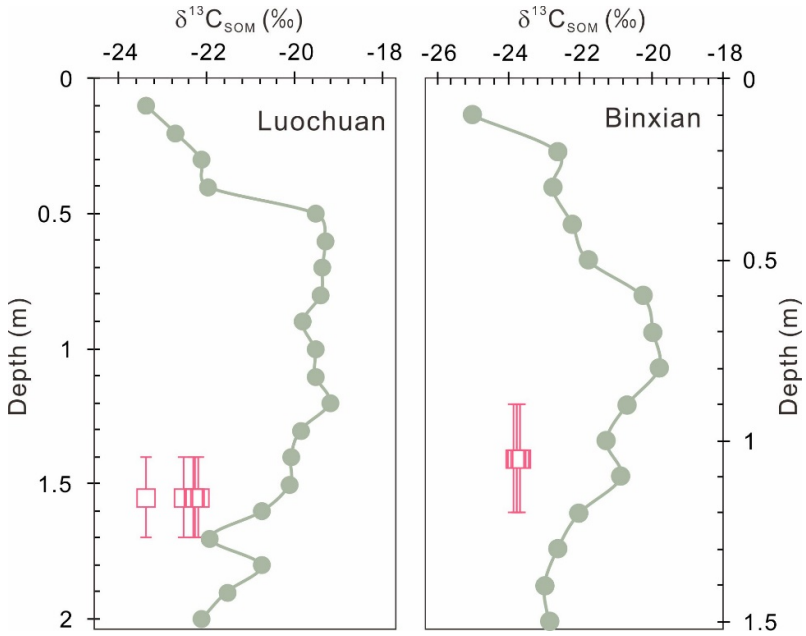

Fig. DR5. Depth profile of $\delta^{13}C_{SOM}$ for the two Holocene sections. Grey points denote $\delta^{13}C$ values of bulk paleosol organic matter, and $\delta^{13}C$ values of SOM occluded in nodules are represented by pink squares. Error bars show the depth intervals where calcite nodules are outcropped.

References:

An, Z., Yongsong, H., Weiguo, L., Zhengtang, G., Clemens, S., Li, L., Prell, W., Youfeng, N., Yanjun, C., and Weijian, Z., 2005, Multiple expansions of C4 plant biomass in East Asia since 7 Ma coupled with strengthened monsoon circulation: Geology, v. 33, no. 9, p. 705-708.

Bowen, G. J., and Beerling, D. J., 2004, An integrated model for soil organic carbon and CO_2: Implications for paleosol carbonate pCO_2 paleobarometry: Global Biogeochemical Cycles, v. 18, no. 1.

Breecker, D. O., 2013, Quantifying and understanding the uncertainty of atmospheric CO_2 concentrations determined from calcic paleosols: Geochemistry, Geophysics, Geosystems, v. 14, no. 8, p. 3210-3220.

Burke, K., Williams, J., Chandler, M., Haywood, A., Lunt, D., and Otto-Bliesner, B., 2018, Pliocene and Eocene provide best analogs for near-future climates: Proceedings of the National Academy of Sciences, v. 115, no. 52, p. 13288-13293.

Cerling, T. E., 1984, The stable isotopic composition of modern soil carbonate and its relationship to climate: Earth & Planetary Science Letters, v. 71, no. 2, p. 229-240.

Cerling, T. E., 1991, carbon dioxide in the atmosphere evidence from Cenozoic and Mesozoic paleosols, v. 291, no. 4, p. 377-400.

Cotton, J. M., and Sheldon, N. D., 2012, New constraints on using paleosols to reconstruct atmospheric pCO_2: Geological Society of America Bulletin, v. 124, no. 9-10, p. 1411-1423.

Gu, Z., Liu, Q., Xu, B., Han, J., Yang, S., Ding, Z., and Liu, T., 2003, Climate as the dominant control on C3 and C4 plant abundance in the Loess Plateau: Organic carbon isotope evidence from the last glacial-interglacial loess-soil sequences: Chinese Science Bulletin, v. 48, no. 12, p. 1271-1276.

He, T., Liu, L., Chen, Y., Qiang, X., and Ji, J., 2015, Carbon isotope record of authigenic calcite from the northern Chinese Loess Plateau: Implications for C4 vegetation evolution during Late Miocene Pliocene: Quaternary Sciences, v. 35, no. 4, p. 791-800. (In Chinese)

Ji, J., Ge, Y., Balsam, W., Damuth, J. E., and Chen, J., 2009, Rapid identification of dolomite

using a Fourier Transform Infrared Spectrophotometer (FTIR): A fast method for identifying Heinrich events in IODP Site U1308: Marine Geology, v. 258, no. 1-4, p. 60-68.

Jiang, W., Peng, S., Hao, Q., and Liu, T., 2002, Carbon isotopic records in paleosols over the Pliocene in Northern China: Implication on vegetation development and Tibetan uplift: Chinese Science Bulletin, v. 47, no. 8, p. 687-690.

Li, G., Chen, J., and Chen, Y., 2013, Primary and secondary carbonate in Chinese loess discriminated by trace element composition: Geochimica et Cosmochimica Acta, v. 103, p. 26-35.

Li, T., and Li, G., 2014, Incorporation of trace metals into microcodium as novel proxies for paleo-precipitation: Earth & Planetary Science Letters, v. 386, no. 1, p. 34-40.

Liu, W., Xiahong, F., Youfeng, N., Qingle, Z., Yunning, C., and Zhisheng, A., 2005, $\delta^{13}C$ variation of C3 and C4 plants across an Asian monsoon rainfall gradient in arid northwestern China: Global Change Biology, v. 11, no. 7, p. 1094-1100.

Lüthi, D., Le Floch, M., Bereiter, B., Blunier, T., Barnola, J.-M., Siegenthaler, U., Raynaud, D., Jouzel, J., Fischer, H., and Kawamura, K., 2008, High-resolution carbon dioxide concentration record 650,000–800,000 years before present: Nature, v. 453, no. 7193, p. 379.

Meng, X., Liu, L., Balsam, W., Li, S., He, T., Chen, J., and Ji, J., 2015, Dolomite abundance in Chinese loess deposits: A new proxy of monsoon precipitation intensity: Geophysical Research Letters, v. 42, no. 23.

Romanek, C. S., Grossman, E. L., and Morse, J. W., 1992, Carbon isotopic fractionation in synthetic aragonite and calcite: Effects of temperature and precipitation rate: Geochimica Et Cosmochimica Acta, v. 56, no. 1, p. 419-430.

Suarez, M. B., Passey, B. H., and Kaakinen, A., 2011, Paleosol carbonate multiple isotopologue signature of active East Asian summer monsoons during the late Miocene and Pliocene: Geology, v. 39, no. 12, p. 1151-1154.

Tipple, B. J., Meyers, S. R., and Pagani, M. J. P., 2010, Carbon isotope ratio of Cenozoic CO_2: A comparative evaluation of available geochemical proxies, v. 25, no. 3.

Yang, S., Ding, Z., Li, Y., Wang, X., Jiang, W., and Huang, X., 2015, Warming-induced

northwestward migration of the East Asian monsoon rain belt from the Last Glacial Maximum to the mid-Holocene: Proceedings of the National Academy of Sciences, v. 112, no. 43, p. 13178-13183.

An, Z., Huang, Y., Liu, W., Guo, Z., Clemens, S., Li, L., Prell, W., Ning, Y., Cai, Y., and Zhou, W., 2005, Multiple expansions of C4 plant biomass in East Asia since 7 Ma coupled with strengthened monsoon circulation: Geology, v. 33, no. 9, p. 705-708.

Bowen, G. J., and Beerling, D. J., 2004, An integrated model for soil organic carbon and CO2: Implications for paleosol carbonatepCO2paleobarometry: Global Biogeochemical Cycles, v. 18, no. 1, p. n/a-n/a.

Breecker, D. O., 2013, Quantifying and understanding the uncertainty of atmospheric CO2concentrations determined from calcic paleosols: Geochemistry, Geophysics, Geosystems, v. 14, no. 8, p. 3210-3220.

Burke, K., Williams, J., Chandler, M., Haywood, A., Lunt, D., and Otto-Bliesner, B., 2018, Pliocene and Eocene provide best analogs for near-future climates: Proceedings of the National Academy of Sciences, v. 115, no. 52, p. 13288-13293.

Cerling, T. E., 1984, The stable isotopic composition of modern soil carbonate and its relationship to climate: Earth & Planetary Science Letters, v. 71, no. 2, p. 229-240.

-, 1991, carbon dioxide in the atmosphere evidence from cenozoic and mesozoic paleosols.

Cotton, J. M., and Sheldon, N. D., 2012, New constraints on using paleosols to reconstruct atmospheric pCO2: Geological Society of America Bulletin, v. 124, no. 9-10, p. 1411-1423.

Ding, Z., Xiong, S., Sun, J., Yang, S., Gu, Z., and Liu, T., 1999, Pedostratigraphy and paleomagnetism of a~ 7.0 Ma eolian loess–red clay sequence at Lingtai, Loess Plateau, north-central China and the implications for paleomonsoon evolution: Palaeogeography, Palaeoclimatology, Palaeoecology, v. 152, no. 1-2, p. 49-66.

Gu, Z., Liu, Q., Xu, B., Han, J., Yang, S., Ding, Z., and Liu, T., 2003, Climate as the dominant control on C 3 and C 4 plant abundance in the Loess Plateau: Organic carbon isotope evidence from the last glacial-interglacial loess-soil sequences: Chinese Science Bulletin, v. 48, no. 12, p. 1271-1276.

He, T., Chen, Y., Balsam, W., Sheng, X., Liu, L., Chen, J., and Ji, J., 2012, Distribution and origin of protodolomite from the late Miocene□Pliocene Red Clay Formation, Chinese Loess Plateau:

Geochemistry, Geophysics, Geosystems, v. 13, no. 6.

He, T., Liu, L., Chen, Y., Qiang, X., and Ji, J., 2015, Carbon isotope record of authigenic calcite from the northern Chinese Loess Plateau: Implications for C4 vegetation evolution during Late Miocene Pliocene: Quaternary Sciences, v. 35, no. 4, p. 791-800.

Ji, J., Ge, Y., Balsam, W., Damuth, J. E., and Chen, J., 2009, Rapid identification of dolomite using a Fourier Transform Infrared Spectrophotometer (FTIR): A fast method for identifying Heinrich events in IODP Site U1308: Marine Geology, v. 258, no. 1-4, p. 60-68.

Jiang, W., Peng, S., Hao, Q., and Liu, T., 2002, Carbon isotopic records in paleosols over the Pliocene in Northern China: Implication on vegetation development and Tibetan uplift: Chinese Science Bulletin, v. 47, no. 8, p. 687-690.

Li, G., Chen, J., and Chen, Y., 2013, Primary and secondary carbonate in Chinese loess discriminated by trace element composition: Geochimica et Cosmochimica Acta, v. 103, p. 26-35.

Li, T., and Li, G., 2014, Incorporation of trace metals into microcodium as novel proxies for paleo-precipitation: Earth & Planetary Science Letters, v. 386, no. 1, p. 34-40.

Lisiecki, L. E., and Raymo, M. E., 2005, A Pliocene□Pleistocene stack of 57 globally distributed benthic δ18O records: Paleoceanography, v. 20, no. 1.

Liu, W., Xiahong, F., Youfeng, N., Qingle, Z., Yunning, C., and Zhisheng, A., 2005, δ13C variation of C3 and C4 plants across an Asian monsoon rainfall gradient in arid northwestern China: Global Change Biology, v. 11, no. 7, p. 1094-1100.

Lüthi, D., Le Floch, M., Bereiter, B., Blunier, T., Barnola, J.-M., Siegenthaler, U., Raynaud, D., Jouzel, J., Fischer, H., and Kawamura, K., 2008, High-resolution carbon dioxide concentration record 650,000–800,000 years before present: Nature, v. 453, no. 7193, p. 379.

Meng, X., Liu, L., Balsam, W., Li, S., He, T., Chen, J., and Ji, J., 2015, Dolomite abundance in Chinese loess deposits: A new proxy of monsoon precipitation intensity: Geophysical Research Letters, v. 42, no. 23.

Romanek, C. S., Grossman, E. L., and Morse, J. W., 1992, Carbon isotopic fractionation in synthetic aragonite and calcite: Effects of temperature and precipitation rate: Geochimica Et Cosmochimica Acta, v. 56, no. 1, p. 419-430.

Rutter, N., Zhongli, D., Evans, M., and Tungsheng, L., 1991, Baoji-type pedostratigraphic section, Loess Plateau, north-central China: Quaternary Science Reviews, v. 10, no. 1, p. 1-22.

Suarez, M. B., Passey, B. H., and Kaakinen, A., 2011, Paleosol carbonate multiple isotopologue signature of active East Asian summer monsoons during the late Miocene and Pliocene: Geology, v. 39, no. 12, p. 1151-1154.

Tipple, B. J., Meyers, S. R., and Pagani, M., 2010a, Carbon isotope ratio of Cenozoic CO2: A comparative evaluation of available geochemical proxies: Paleoceanography, v. 25, no. 3.

Tipple, B. J., Meyers, S. R., and Pagani, M. J. P., 2010b, Carbon isotope ratio of Cenozoic CO2: A comparative evaluation of available geochemical proxies, v. 25, no. 3.

Yang, S., Ding, Z., Li, Y., Wang, X., Jiang, W., and Huang, X., 2015, Warming-induced northwestward migration of the East Asian monsoon rain belt from the Last Glacial Maximum to the mid-Holocene: Proceedings of the National Academy of Sciences, v. 112, no. 43, p. 13178-13183.